O. E. Osafile[1] and R. Ocaya[2]

Investigation of the Phonon, Optical, and Thermoelectric Properties of Carbon-based Half Heusler Alloys for solar cell applications

[1]Department of Physics, Federal University of Petroleum Resources, PMB 1221, Effurun, Nigeria
[2]Faculty of Natural and Agricultural Sciences, University of the Free State, PO Box 339, Bloemfontein 9300, Republic of South Africa
*Corresponding author's E-mail address: osafile.omosede@fupre.edu.ng

Abstract - Viable solar energy materials for solar cell application are on the front burner for researchers in material science due to the world energy crisis. We investigated the structural, electronic, phonon, and transport properties of ScAgC half Heusler alloy using the density functional theory based on the Purdue-Burke-Enzerhof generalized gradient approximation and HSE hybrid exchange-correlation functional implemented in quantum espresso. The band gap, lattice constant, and other structural and electronic property results obtained compare well with results from previous work. The hole and electron doping and carrier concentrations suggest that ScAgC is a better thermoelectric material and an n-type semiconductor. The optical properties show a high absorption coefficient, which increased from 7 × 104 cm−1 to 39 × 104 cm−1 through the visible light region. The high reflectivity exceeds 30% in the visible region and supports the use of ScAgC alloy in optoelectronic applications, solar and photovoltaic cells. The plasmon frequency for ScAgC alloy is 14.49 eV supporting its application as a solar cell material. The alloy is stable at low/medium temperatures but unstable at high temperatures. The clear wide phonon band gap between the acoustic and optical branches supports a strong ionic bonding that suggests the material is rigid.

Keywords: Density functional theory, optical properties, Half-Heusler alloys, phonon properties, Thermoelectric properties.

1.0 Introduction

Alternative and clean energy is a global need. Despite energy deficiency, the pollution from fossil fuel use for energy generation results in ozone layer depletion and global warming. Hence, clean energy research has taken center stage in the search for a sustainable energy supply. Therefore, it is necessary to identify efficient, available, and cost-effective materials that can push down the cost of production without compromising efficiency to make energy sustainable.

Researchers have proposed several designs, like heterojunctions, as innovative solutions to enhance the energy output from solar cells [1-3]; as good as this is, there is also the need to explore the option of tuning materials through doping or element replacement. Semiconductor materials like silicon have contributed immensely to commercial scaling in solar energy supply. However, silicon is not naturally found in the needed form and requires a rigorous purification process. For example, a furnace temperature of about 2000^{o}C is required to obtain refined silicon of approximately 99.9% purity. These high temperatures will emit greenhouse gases that are not environmentally safe, and the rigidity of the cells makes the end-of-life disposal of solar panels an environmental threat. In addition, researchers observed that silicon-based solar cells had been stuck at efficiencies of approximately 22% for the past decade. The rigidity of the cells also makes manipulative use almost impossible[4]. These failures create research gaps that need to be bridged. Bridging the gap requires searching for alternative semiconductor materials whose properties can be tuned through doping to enhance and scale the power conversion efficiency of generated solar cells. A commercially viable solar cell must have a power conversion efficiency of over 15%, low production cost, and a long-life span [5].

Among several semiconductors promoted by researchers, semiconductors belonging to the family of Heusler alloys prove to deserve further research. Heusler alloys are a family of alloys that was first proposed by Heusler [6]. A half-Heusler (HH) variant was later reported by Groot et al. [7]. The half-Heusler variant with eight valence electron counts has attracted much research attention when it applies to solar energy materials because the structure can be tuned to match the structural configuration of fundamental semiconductor materials like silicon, germanium, and GaAs [8]. The band gap of these alloys can also be easily tuned when the chemical composition is changed; this aims to ensure we have the desired properties. The idea is to retain the effective structural composition of the conventional silicon or GaAs semiconductor. Hence, as seen in GaAs, the eight valence electrons will be shared among three atoms as against two. The third atom is at the octahedral vacancy in the ZnS-type lattice. This fact automatically leads to the formation of a rocksalt-like sublattice characterized by ionic bonding interaction [8]. Half Heusler alloy falls in the category of inorganic or crystalline semiconductors. Some of the attractions of HH alloys are that they can be easily fabricated, and the elements are inexpensive and abundant in nature [9].

Valence count can predict specific properties of HH semiconductors, and they obey the Slater-Pauling rule that says that 8, 18, or 24 valence electron compounds can be largely predicted to be semiconductors. Hence, HH alloys with eight valence counts are expected to be semiconductors. Possible structural classifications are determined by the number of electrons in the atom's outermost shell, including combinations such as I-II-V, II-III-III, I-I-VI, and II-II-IV [10]. Mehnane et al. studied 36 I-II-V semiconductor materials. They compared the electronic structure with II-VI semiconductors by investigating their lattice parameters, band gaps, and static dielectric constants at ambient pressure. Their report shows that LiCaN, NaCaN, and NaMgAs HH alloys possess the properties needed for application in optoelectronic devices [11]. Kacimi et al. studied 96-eight valence electron semiconductors in various categories using the full-potential (linear) augmented plane-wave plus local orbitals method. They identified four I-III-IV compounds (NaAlC, NaGaSi, NaInSi, and KAlC) that exhibited properties relevant to optoelectronic applications [12]. Using the full-potential linearized augmented plane wave (FP-LAPW) method as implemented in the WIEN2K code, Belmiloud et al. proposed that ScAgC, YCuC, CaZnC, NaAgO, and LiCuS could be strong candidates for photovoltaic applications in multi-junction devices [13]. Belmiloud et al. allege that there is clear evidence of staggered-alignment type-II obtained for ScAgC, YCuC, CaZnC, and (LiCuS)/GaAs(Si), indicating a large splitting of electron and hole pairs created at the GaAs (Si) edge of the structure. One of the attractions of the I-III-IV compounds is the lattice match between the compounds and that of GaAs semiconductors: such match opens possibilities for improvements in the thermoelectric, optical, and phonon properties expected for semiconductors applicable to solar cells. To our knowledge, however, there is one report in the literature on the optical and thermoelectric properties of ScAgC half Heusler alloy. Furthermore, the atomic mass difference between the atoms needs the investigation of the spin-orbit coupling to understand its effect on the band gap and other properties of the compounds; this was not factored into the reports in the existing literature.

In this work, we investigate the structural, electronic, and lattice dynamical properties of ScAgC I-III-IV compounds with and without spin coupling from first principles using the quantum espresso software. We also investigate the thermoelectric and optical properties of the alloys using the density functional perturbation theory. In section 2 of this article, we present the methodology for this work in detail; we present and discuss the results in section 3 and conclude thereafter.

2.0 Computational method

Using the quantum espresso code (QE) [14], we studied the structural, electronic, thermoelectric, and phonon properties of ScAgC half Heusler alloy from the first principles. The potentials for calculations were constructed using the projector augmented wave (PAW) [15, 16] method, and the generalized gradient approximation (GGA) was employed to treat the Perdew-Burke-Erzhenhof exchange correlation between electrons [17]. We used the Monkhorst-Pack scheme [18] to construct an 8×8×8 grid for the electronic structure calculation. A converged value of 70 eV was used as the kinetic energy cutoff of the plane-wave basis function. We relaxed each atom in the unit cell using the Broyden–Fletcher–Goldfarb–Shanno (BFGS) concept to obtain the equilibrium configuration for the atomic positions. A denser k-point mesh of a (20×20×20) grid with a tetrahedra occupation was used to calculate states' electronic density. We also sampled the alloys' behavior at equilibrium temperature as functions of the volume and pressure by fitting the result obtained from the total energy calculation to the Birch-Murnaghan equation of state [19-21]. As reported in the literature, we treated the compound as a ferromagnetic system in the fcc crystallized phase. We selected dense high symmetry k-points for the FCC structure using (X-window)

Crystalline Structures and Densities (XCrySDen) package [22] for the band structure calculations. We carried out the phonon calculations at the harmonic (volume) and quasiharmonic (volume change) levels using the density functional perturbation theory (DFPT) as described by Togo and Tanaka [23]. We used a plane-wave energy cutoff of 300 eV for the phonon properties and an energy convergence criterion of 10^8 eV. We used a $30 \times 30 \times 30$ k-point sampling mesh for the unit cell and the equivalent density mesh for the supercells with a 0.2 eV smearing width of the Methfessel–Paxton scheme [24]. Supercell and finite displacement approaches were used for the phonon calculations with $2 \times 2 \times 2$ supercells of the primitive unit cell without atomic displacements. We used the Fermi-Dirac distribution to obtain the Fermi level from the electronic density of states. We computed the transport coefficients according to the Boltzmann equation using the constant relaxation time approximation (CRTA), which assumes that the relaxation time is constant regardless of energy.

3.0 Results

3.1 Structural Properties

ScAgC compound crystallizes in the face-centered cubic structure in the space group $F\bar{4}3m$ and space number 216 as a non-magnetic semiconductor. The electronic configuration of the elements investigated is $3d^1 4s^2$ and $5s^1$ for Scandium and silver, respectively, while carbon is $2s^2 2p^2$. The alloy crystallizes in the MgAgAs structure with Ag, C, and Sc atoms occupying the atomic positions (0, 0, 0), (0.25, 0.25, 0.25), and (0.50, 0.50, 0.50), respectively. The equilibrium lattice parameter with and without the spin-orbit coupling in Angstrom is 5.61 and 5.59, respectively. ScAgC alloy obeys the Slater-Pauling rule for hH alloys and crystallizes as a non-magnetic semiconductor. We confirmed this by using the rule for 18 valence electrons $M_t = Z_t - 18$ proposed by Slater & Pauling, where Z_t is the alloy's valence number, and M_t is the magnetic moment per unit formula of the alloy. In our case, Z_t is 18.

The results obtained during lattice optimization for energy and volume are fitted to the Murnaghan equation of state using the following:

$$\Delta E(V) = E - E_0 = BV_0\left[\left(\frac{V_n}{B'}\right) + \left(\frac{1}{1-B'}\right) + \left(\frac{V_n}{B'(B'-1)}\right)\right] \quad [1]$$

Where E_0 and V_0 equilibrium values of energy and volume, respectively, without pressure, while B and B denote the bulk modulus and its derivative. The relationship between the energy and volume is shown in Fig. 1 for the three possible combinations for a half-Heusler alloy. We present values for the bulk modulus, pressure derivative of bulk modulus, volume, ground state energy, energy bandgap, and lattice constant using PBE-GGA in Table 1. The compound's magnetic moments are zero in all three interacting elements confirming its non-magnetic nature.

One test for ascertaining an alloy's structural stability and establishing the possibility of experimental simulation is deduced using the compound's formation energy. Negative formation energy supports simulation, while positive formation energy prohibits experimental simulation. We calculated the formation energy by subtracting the energy of each element from the energy of the bulk compound using the equation; $E_{form} = \frac{1}{3}[E_0 - (E_X + E_Y + E_Z)]$. The formation energy obtained for ScAgC is -4.25 eV showing that the alloy is structurally stable and that experimental simulation is possible.

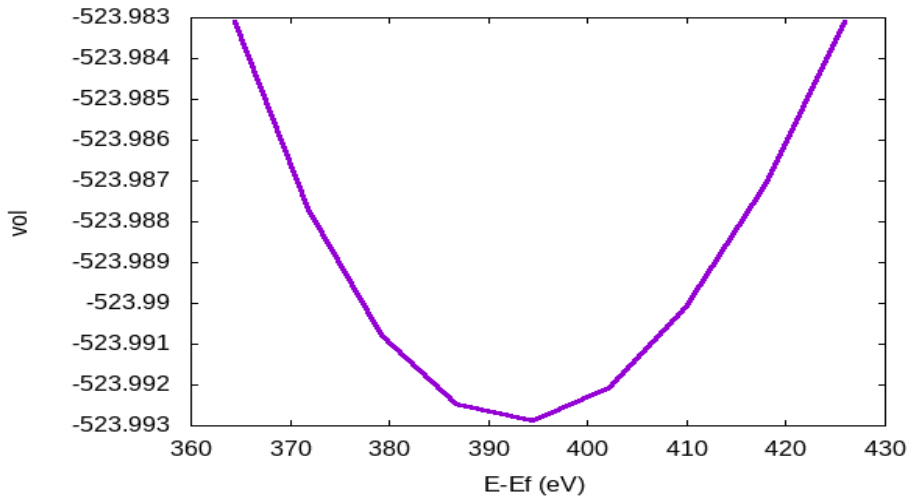

Fig. 1. Lattice optimization for the minimum energy versus volume as fitted to the Murnaghan equation of state.

Table I. Lattice constant *(a_0)*, ground state energy E, bulk modulus B_0 , pressure derivative of the bulk modulus B_0' , volume V_0, formation energy (E_{form}) and energy bandgap (**E_g**) of ScAgC compound in the most stable state using PBE-GGA with and without SOC.

ScAgC	***a_0* (Å)**	**E *(Ry)***	***B_0* (GPA)**	***B_0'***	***V_0* (a.u.)^3**	***E_{form}* (eV)**	**E_g (eV)**
SOC	5.59	-733.61	124.40 128.4	4.68	297.92	-4.25 -5.43	0.49 1.183
Without SOC	5.61 5.60	-530.67	120.20	4.73	294.52		0.46
HSE	5.61						1.33

3.2 Electronic Properties

We present results for the electronic structure of the ScAgC compound, including the density of states (DOS) and electronic band structure calculations using PBE-GGA with and without spin-orbit coupling. PBE-GGA underestimates bandgap. Hence, we also explored the HSE functional to improve the compound's bandgap. The FCC structure's band structure calculation is along the high symmetry path K→Γ→X→W→K→Γ→L with a dense k-point. In Fig 2, we present the band structure and density of states using GGA with and without SOC and HSE functional. We observe steep slopes at the Γ point, the center of the crystal momentum space or k = 0 space, and X (the edge π/L of the first Brillouin zone in the 001 direction) symmetric point. The steep dispersion indicates a stronger orbital interaction arising from the d-orbitals of Sc and Ag, resulting in increased charges' possible mobility. The steeper slope also suggests a covalent bonding between the d^8 orbital of Sc and the d^3 orbital of C.

Furthermore, Γ→X. the bandgap shows that Ni's d states are delocalized in the region of the Fermi energy. On the other hand, we observe shallow or flat bands between W→K, indicating ionicity and low group velocity resulting from the *s* and *p* orbitals' localization. The flat bands in the conduction band occur around 1 eV and 2 eV, while the flat bands appear in the valence band around -1 eV to -3 eV.

Figure 2 also shows the electronic density of states for ScAgC alloy in the non-magnetic state. The shift arising from the effect of the spin-orbit coupling is seen in the electronic density of states. The SOC splits the s, p, and d orbitals of Sc and Ag into two, giving rise to 12 orbitals compared to 6 in calculations without SOC. On the other hand, the s orbital is not split between C, but the p and d orbital again split in two resulting in 5 orbitals compared to the three seen in computations without SOC. The size of the bandgap supports possible charge mobility.

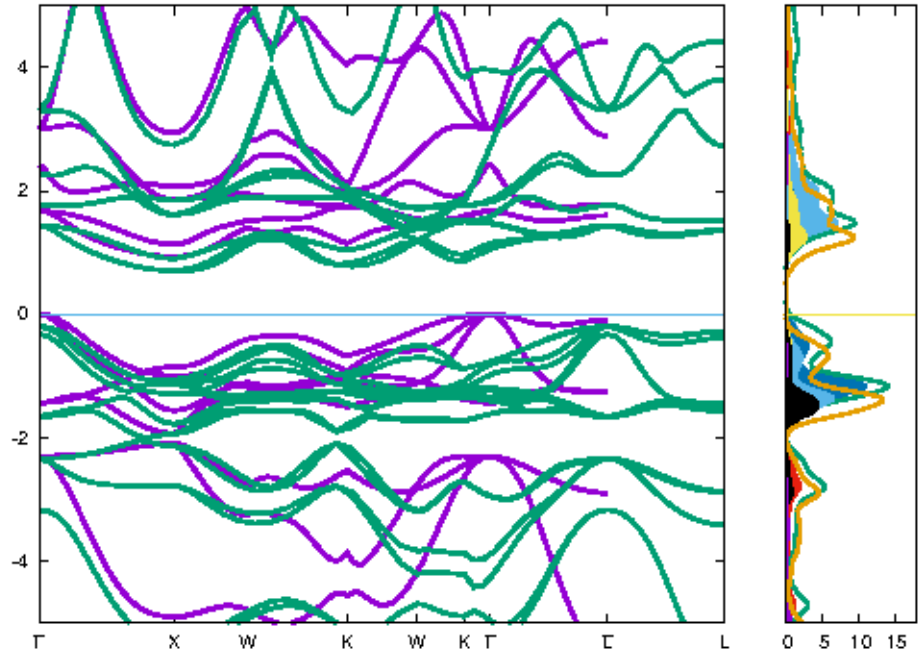

Fig. 2. Electronic band structure and density of states of ScAgC with and without SOC using PBE-GGA

3.3 Thermoelectric Properties

We have calculated the power factor per unit relaxation time, electrical conductivity per unit relaxation time, and the Seebeck coefficient at temperatures of 300 K, 600 K, 900 K, and 1200 K versus the chemical potential dependence of ScAgC hH alloy without SOC. The efficiency of a thermoelectric material (TEM) is computed using the dimensionless figure of merit described by the relation $ZT = \frac{S^2\sigma}{\kappa}T$. S and T represent the Seebeck coefficient and absolute temperature, respectively, while σ and κ are the electrical and lattice conductivity, respectively. The mutual dependence of the parameters requires that the material have a high-power factor and a low thermal conductivity for a TEM to perform optimally. We obtain the relation for the power factor using $\sigma S^2[W\,/\,m\,/\,K^2]$ where σ and S^2 retain their usual meaning.

In figure 3, we show results for the power factor per unit relaxation time, electrical conductivity per unit relaxation time, and Seebeck coefficients as functions of the free carrier concentration for both n-type and p-type phases. The Seebeck coefficient peaks at $1500\,\mu V.K^{-1}$ with a free carrier coefficient of -0.03 cm^{-3} for both n and p types at a temperature of 300 K. At the same temperature, the electrical conductivity per unit relaxation time also attains a peak of $54 \times 10^{19}\,/\,cms$ for the hH alloy with SOC at -0.1 cm^{-3}. For the power factor, however, the highest peak for calculations with SOC is obtained at a high

temperature of 1200 K and free carrier concentration of -0.075 cm^{-3}. The Seebeck coefficient attenuates to zero with the increase in carrier concentration.

We, however, observe a different behavior for calculations without SOC. The peak of the electrical conductivity per unit relaxation time, as shown in Figure 4, is shifted from -0.1 cm^{-3} to -0.025 cm^{-3} at 300 K, indicating that a lower concentration is required at moderate temperature to increase the electrical conductivity. The maximum value of the electrical conductivity is reduced to about $30 \times 10^{19} / cms$. On the other hand, the peak of the Seebeck coefficient is shifted from -0.03 cm^{-3} to 0.04 cm^{-3}, hence promoting the p-type semiconductor, with the Seebeck coefficient increasing from 1500 $\mu V.K^{-1}$ to 1700 $\mu V.K^{-1}$. The power factor is shifted to around the Fermi level at zero, and we see the peak around zero concentration to be. From the results, we can conclude that consideration of the SOC enhances the transport properties of the alloy because there is a marked increase in the power factor per relaxation time from the conduction band in calculations without SOC to the valence band in calculations with SOC. Hence, making it a P-type semiconductor

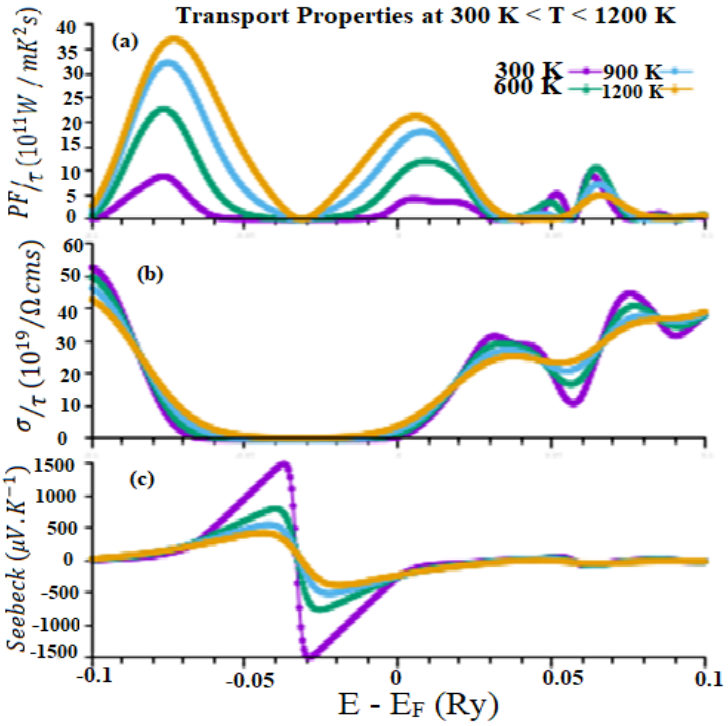

Figure 3. The (a) power factor per unit relaxation time, (b) electrical conductivity per unit relaxation time, and (c) Seebeck coefficient at temperatures of 300 K, 600 K, 900 K, and 1200 K versus chemical potential dependence of ScAgC hH alloy with SOC.

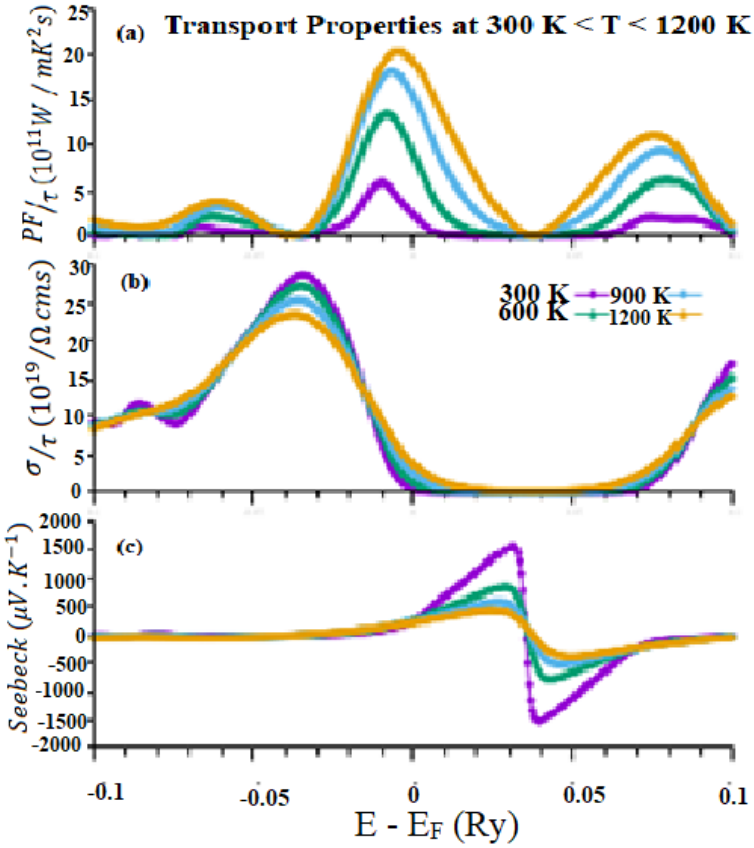

Figure 4. The (a) power factor per unit relaxation time, (b) electrical thermal conductivity per unit relation time, and (c) Seebeck coefficient at temperatures of 300 K, 600 K, 900 K, and 1200 K versus chemical potential dependence of ScAgC hH alloy without SOC.

3.4 Optical Properties

The permittivity of material measures the amount of charge required to generate a unit of electric flux. The permittivity, in this case, is described by the real and imaginary part of the dielectric function (ε), also known as the frequency-dependent complex dielectric function. The light frequency-dependent complex dielectric function is described by the relation $\varepsilon(\omega) = \varepsilon_{1(\omega)} + \varepsilon_2(\omega)$. Where $\varepsilon_{1(\omega)}$ is the real part which scientifically measures the polarization of the material interaction with light, and the imaginary part $\varepsilon_{2(\omega)}$ predicts the energy loss propensity of the material. We have investigated the optical properties of ScAgC hH alloy based on PBE-GGA by computing the permittivity through the Kohn and Sham orbital transition matrix elements using modulo-conserving pseudopotentials and gaussian smearing of 0.1 eV. The method adopted obtains the dielectric constant by calculating the dipole transitions between the energy levels. The calculation produces the imaginary part of the dielectric constant; we obtain the real part of the dielectric constant through the Kramer-Kronig relations given as

$$\varepsilon_1(\omega) = 1 + \frac{2}{\pi} P \int_0^{\infty} \frac{\omega' \varepsilon_2(\omega')}{\omega'^2 - \omega^2} d\omega \qquad [2]$$

$$\varepsilon_2(\omega) = -\frac{2\omega}{\pi} P \int_0^{\infty} \frac{\varepsilon_1(\omega') - 1}{\omega'^2 - \omega^2} d\omega' \qquad [3]$$

Where $\omega'(\omega)$ is the angular optical frequency for the imaginary and real parts, respectively, while P is the carefully selected Cauchy principal value. After obtaining the optical frequency dielectric functions, other essential properties can be calculated directly from the results.

Such properties include the absorption coefficient (α) and the extinction coefficient (κ). Other relevant properties are the reflectivity (R), the real and imaginary parts of the refractive index (n), and the electron energy loss function (L). The mathematical relations required to obtain these properties are captured in equations [4] to [8]. We carried out all calculations between 0 and 15 eV. Another vital parameter derived from the calculations performed is the plasmon frequency (ω_P); it is the characteristic frequency at which the semiconductor material changes from a metallic material to a dielectric; this value coincides with the zero-frequency of the real part of the dielectric functions [55]. For example, the plasmon frequency for ScAgC alloy is 14.49 eV.

$$n = \left[\frac{1}{2}\sqrt{\varepsilon_1^2 + \varepsilon_2^2} + \frac{\varepsilon_1}{2}\right]^{\frac{1}{2}} \quad [4]$$

$$\kappa = \left[\frac{1}{2}\sqrt{\varepsilon_1^2 + \varepsilon_2^2} - \frac{\varepsilon_1}{2}\right]^{\frac{1}{2}} \quad [5]$$

$$R = \frac{(1-n^2)+\kappa^2}{(1+n^2)+\kappa^2} \quad [6]$$

$$L = \frac{\varepsilon_2}{\varepsilon_1^2+\varepsilon_2^2} \quad [7]$$

$$\alpha = \sqrt{2}\omega\left[\sqrt{\varepsilon_1^2 + \varepsilon_2^2} - \varepsilon_1\right]^{\frac{1}{2}} \quad [8]$$

For improved efficiency, researchers propose that solar cells absorb light in the visible region; however, further research has proved that solar cells also absorb light in the infrared and ultraviolet regions. Solar cells can absorb light between the wavelengths of 400 and 1000 nm. The energy of the visible spectrum is in the range of 3 eV to 1.5 eV in the violet and red sides, respectively, at a frequency of 10^{14} Hz, while the energy of the ultraviolet region falls between 3 eV and 30 eV. The optical investigation results show that ScAgC absorbs light in the ultraviolet and visible regions.

We present the results for the optical properties calculations in Figures 5 to 10. From the results, ScAgC alloy exhibits a peak performance in the ultraviolet region at a wavelength between I nm and 400 nm. Furthermore, the results for the optical properties are in good agreement with the results from the work of Vinod et al., where they carried out a density functional theory calculation as implemented in ABINIT.

Figure 5 shows the refractive index of the real and imaginary parts of the alloy. The alloy has a refractive index of 0 and 4 at a frequency of 0 eV in the imaginary and real parts, respectively. A maximum peak of 5.5 and 3.2 is seen at 2 eV and 2.2 eV for the real and imaginary parts, respectively. Other peaks arising from intraband transitions are also visible. The result shows a high probability of electron mobility in the material. Recall that the imaginary part describes the polarization when light hits the material's surface. The 3.2 peak at 2.2 eV in the imaginary part shows that light will be absorbed more than refracted because the higher the refractive index, the slower the light travels; this light will travel at approximately 31.25% of the speed of light in air.

Figure 6 shows the real and imaginary parts of the optical dielectric functions. The real part shows a polarization of 15.87 at 0 eV and a peak polarization of 28.15 at 1.95 eV. There is a sharp decline from the peak value of 28.15 at 1.95 eV to 0.97 at 2.73 eV. The region of sharp decline describes the anomalous dispersion region and comes at a high energy dissipation. The real part attains zero dielectric constants at 3.48 eV, 4.03 eV, and 4.83 eV and attenuates to zero at 14.37 eV. A negative peak is evident at 4.75 at 5.5 eV, describing the very low frequency at which the material behaves as metal.

On the other hand, there is no polarization at 0 eV at the imaginary part of the frequency, and the maximum peak absorption of 23.95 is seen at 2.63 eV; other peaks are also between 3.6 eV and 8 eV and then a steady attenuation to 0 at 13.57 eV. The result shows that the material

will store and remit more energy permanently than it will absorb. Furthermore, the negative value of the real part shows metallic behavior within the visible and ultraviolet regions.
Figure 7 shows the reflectivity of the material. The sum of reflection and transmission gives the ideal index of vacuum space. At 0 frequency, we have a 35.8% reflectivity and a transmission of 64.2%. However, the highest reflectivity(transmission) of 57.6% (42.4%) is at 2.1 eV. We also observe a 100% (0%) transmission (reflection) occurs at 12.84 eV. The absorption coefficient is the cross-sectional area per unit volume of the material and depends on frequency. It occurs when the incident light and material are resonant. Figure 8 shows the highest absorption at 6.43 cm^{-1} at a frequency of 2.68 eV. The result suggests that at a frequency of about 462 nm, light can penetrate a depth of 6.43 cm^{-1} before absorption. The transmission electron energy loss (EEL) defines the kinetic energy change of the electron that results from the inelastic interaction of the material with light. It measures the plasmon and inter-band transitions. Figure 9 shows that the zero-loss peak is 19.34 at 14.4 eV. The result classifies the loss as the low-loss spectrum, which falls between 0 and 50 eV. The plasmon peaks are at 1.97 and 10.29 at frequencies of 11.59 eV and 14.02 eV, respectively.

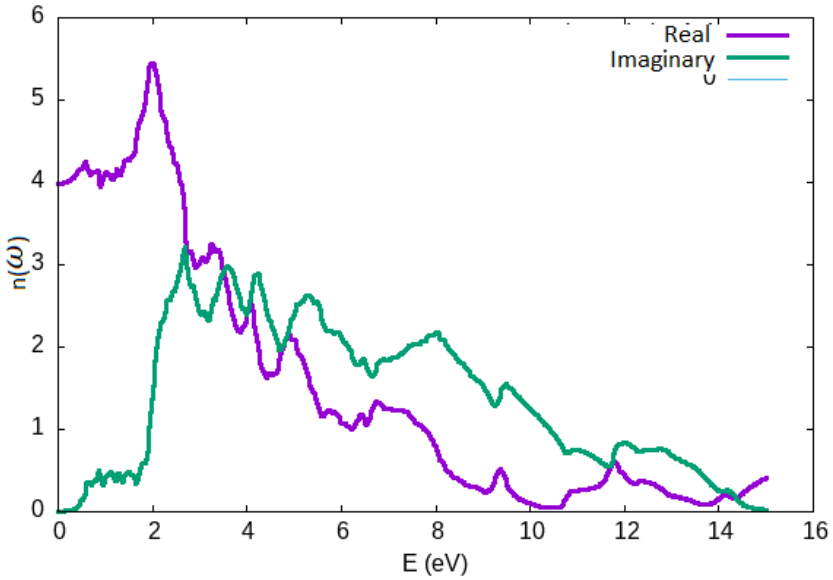

Figure 5. The refractive index of ScAgC half Heusler alloy for the real and imaginary parts using DFT-GGA

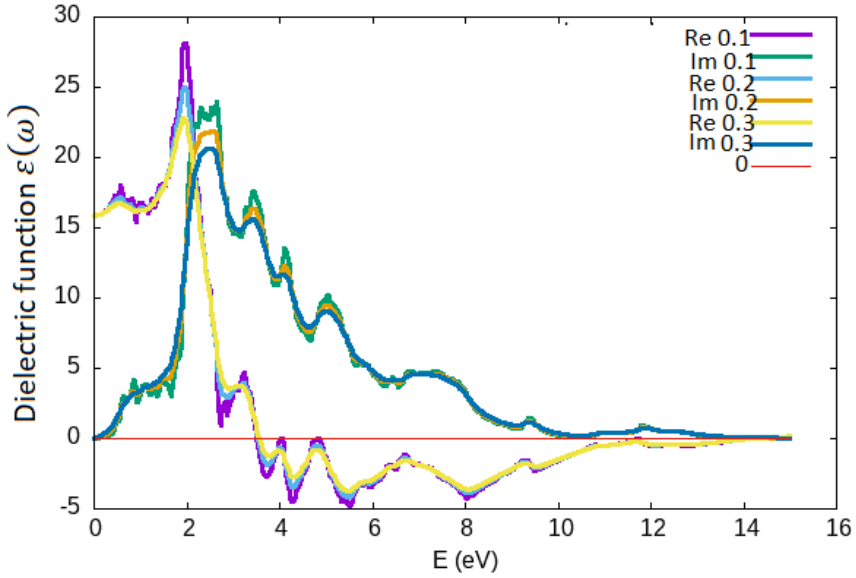

Figure 6. The dielectric function of ScAgC half Heusler alloy for the real and imaginary parts using DFT-GGA

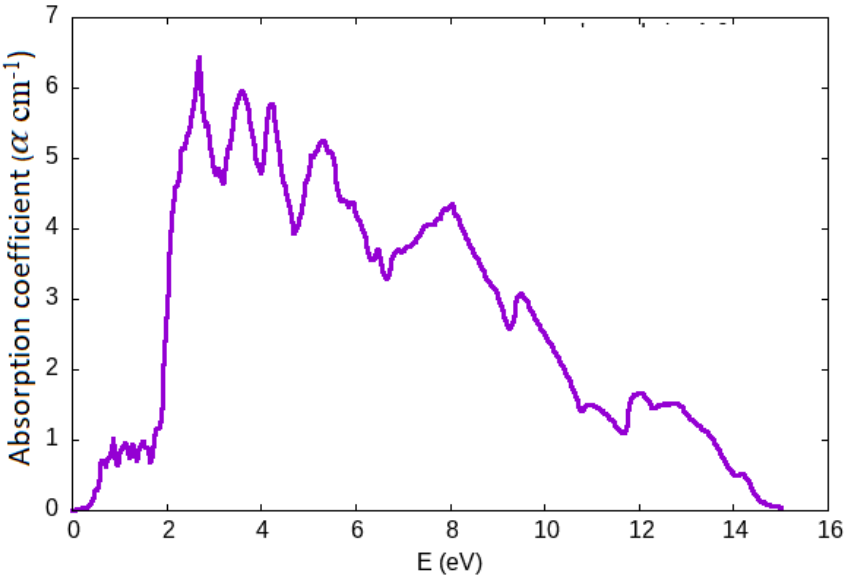

Figure 7. The absorption coefficient of ScAgC half Heusler alloy using DFT-GGA

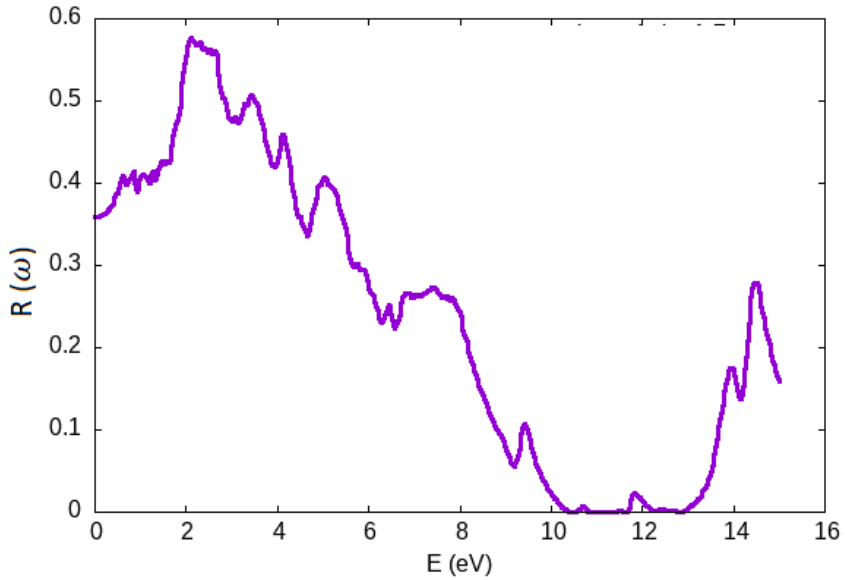

Figure 8. The reflectivity of ScAgC half Heusler alloy using DFT-GGA

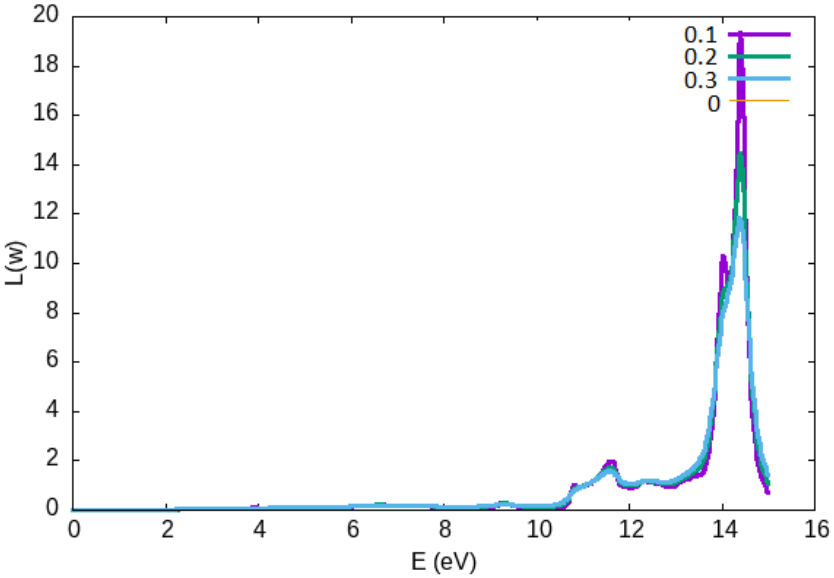

Figure 9. The electron energy loss spectrum of ScAgC half Heusler alloy for 0.1, 0.2, and 0.3 smearings using DFT-GGA

3.5 Lattice dynamics, Phonon, and Thermodynamic Properties

Four fundamental thermodynamic potentials explain a material's state, behaviour, and possible applications; these properties include enthalpy, internal energy, Gibbs free energy, and Helmholtz free energy. In addition, other properties are vital to understanding the material's behavior when interacting with temperature changes arising from the environment. Parameters that affect the thermodynamic properties of materials include chemical and atomic composition, atomic interactions, electronic and photonic charge interactions, crystalline architecture, and temperature change. Hence, we present results for the thermodynamic and phonon properties of ScAgC hH alloy from first principles at 0 K, 12 K, 300 K, and 1596 K. The results focus on the entropy due to temperature change, the specific heat capacity, and the relationship with the Dulong-Petite law. The specific heat capacities at constant temperature and pressure significantly contribute to a crystal material's thermal

diffusion or conduction. We investigated the material's thermal properties using the density functional perturbation theory in the quasiharmonic Debye model approach. The Debye model provides relations for the heat capacity at constant volume, entropy as a function of temperature increase, Helmholtz free energy, and linear thermal expansivity using the following relations;

$$C_{\upsilon} = 3nk\left[4D\left(\frac{\Theta}{T}\right) - \frac{3\Theta/T}{e^{\Theta/T}-1}\right] \quad 9$$

$$S(T) = nk\left[4D\left(\frac{\Theta}{T}\right) - 3In\left(1-e^{-\Theta/T}\right)\right] \quad 11$$

$$A(T) = nkT\left[\frac{9}{8}\left(\frac{\Theta}{T}\right) - 3In\left(1-e^{-\Theta/T}\right) - D\left(\Theta/T\right)\right] \quad 12$$

$$\alpha = \frac{\gamma C_{\nu}}{B_T V} \quad 13$$

First, we calculated the phonon dispersion properties at low and high temperatures. There are three atoms in the unit cell of the alloy. Hence, as we expect, nine dispersion branches (three optical and six acoustic branches) at Γ can interact with light. ScAgC alloy is dynamically stable at low temperatures and zero pressure but loses its dynamical stability at high temperatures. Hence, there are negative frequencies in the phonon dispersion curves at a temperature of 1596 K. To promote convergence, we built a $4 \times 4 \times 4$ supercell and carried out all calculations in the first Brillouin zone, representing the primitive cell (not conventional cell) in the reciprocal lattice. The zones sampled in this work cover Γ – X – K – Γ - L – W – X. the alloy proves to be dynamically stable at zero pressure and low temperature; we observe nine modes in the phonon dispersion spectra in Figs. 10 (a, b); The optical mode for ScAgC is between 470 to 500 cm^{-1}; this puts the wavelength of the alloy in the Far-IR wavelength region.

Table II. Thermodynamic properties of ScAgC compound at different temperatures

T (K)	***V (a.u)³***	**C_V *(J/Kmol)***	**Θ_D (K)**
0	296.65	-	-
12	298.70	-	-
300	300.68	65.36	387.28
1596	304.58	73.43	404.25

From Figure 10, a clear gap appears between the acoustic and optical modes and another gap between the two optical modes for the alloy. The highest transverse acoustic (TA) branch is between Γ and X. There is a triple degeneracy at Γ in both modes; this gives rise to one longitudinal optical (LO) phonon and two transverse optical (TO) phonon splitting at Γ. LO-TO splitting removes degeneracy between the LO and TO phonons at the center of the Brillouin zone. The LO-TO splitting aids in evaluating the strength of ionic bonding in a material. From the behavior of the alloy, the ionic bond between the atoms is strong enough to reduce the vibration that occurs.

The Debye temperature Θ_D explicitly explains the difference between low and high-temperature zones of an alloy. We computed the Debye temperature using Eqn. 14, Where h is Planck's constant, K_B is Boltzmann's constant, n is the number of atoms per unit cell, N_A is Avogadro's number, ρ is density, and M is the molecular weight and ν_m is the sound velocity at zero pressure.

$$\Theta_D = \frac{h}{K_B}\left[\frac{3n}{4\pi}\frac{N_A\rho}{M}\right]^{1/3}\nu_m \qquad (14)$$

A higher Θ_D supports the possibility of higher thermal conductivity and is a reliable check-off for structural rigidity and material with higher Θ_D will have higher-energy phonon modes, which decrease the chances of non-radiative relaxation [56,57]. Non-radiative relaxation enhances device performance and quantum coherence in solar cells [58].
ScAgC alloy has a Θ_D 404.25 K at zero pressure is higher than Θ_D for most eight-electron hH alloys like BiBaK, BiKSr, XNbSn, and BiLiSr [59, 60].

Table II shows that the heat capacity is only measurable at 300 K and above. As the temperature increases, the volume of the compound also increases slightly, leading to an area and volume expansion. The law of Dulong-Petit prohibits a change in the product of a crystal element's specific heat capacity and mass per mole. Compliance with the law of Dulong and Petit for ScAgC alloy occurs at 74 J/Kmol and a temperature of 720 K. The entropy in Fig. 11 (a) increases with temperature to 210 J/K at a maximum temperature of 1596 K. While the Helmholtz free energy decreases with temperature increase as seen in Fig. 11c with a minimum of -530.842 Ry at 1596 K.

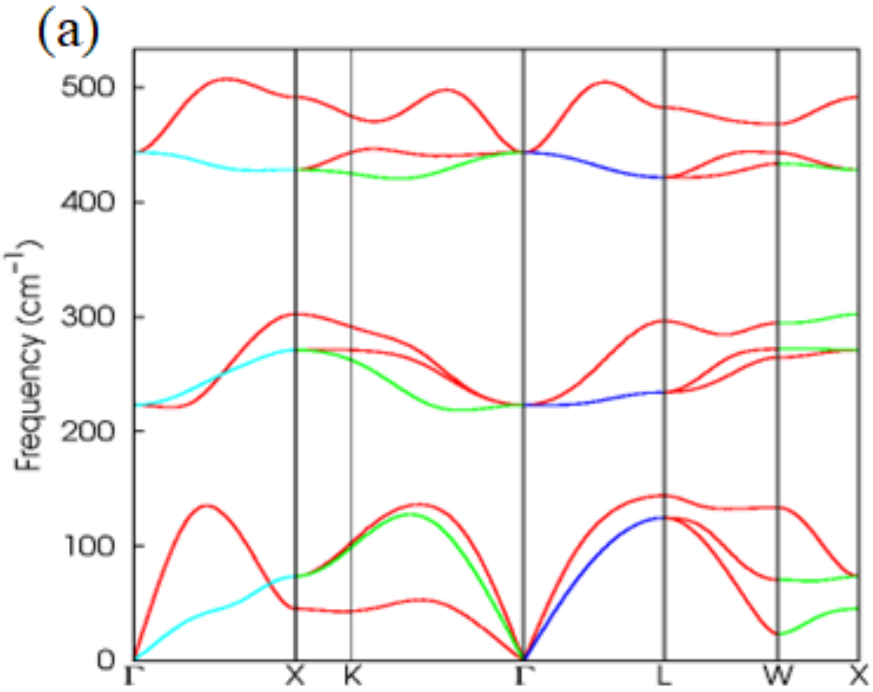

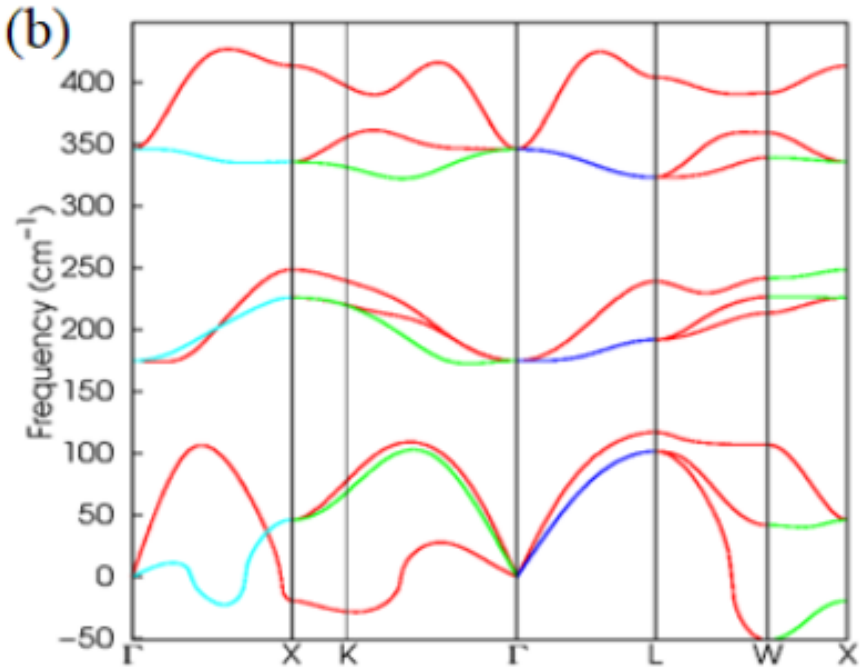

Fig. 10 phonon dispersion curves of ScAgC half Heusler alloy at (a) 300 K and (b) 1596 K

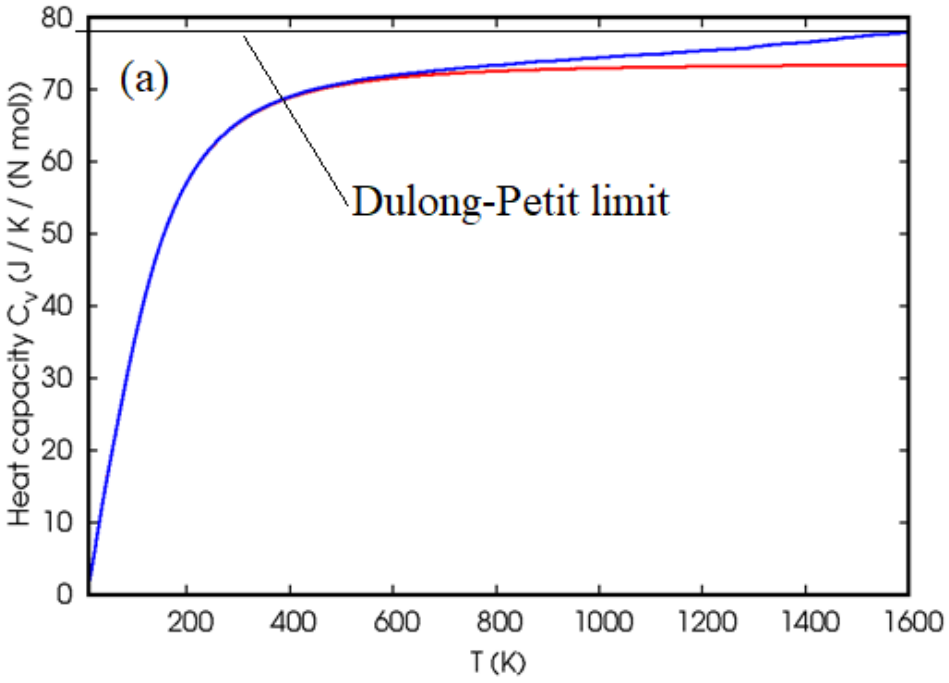

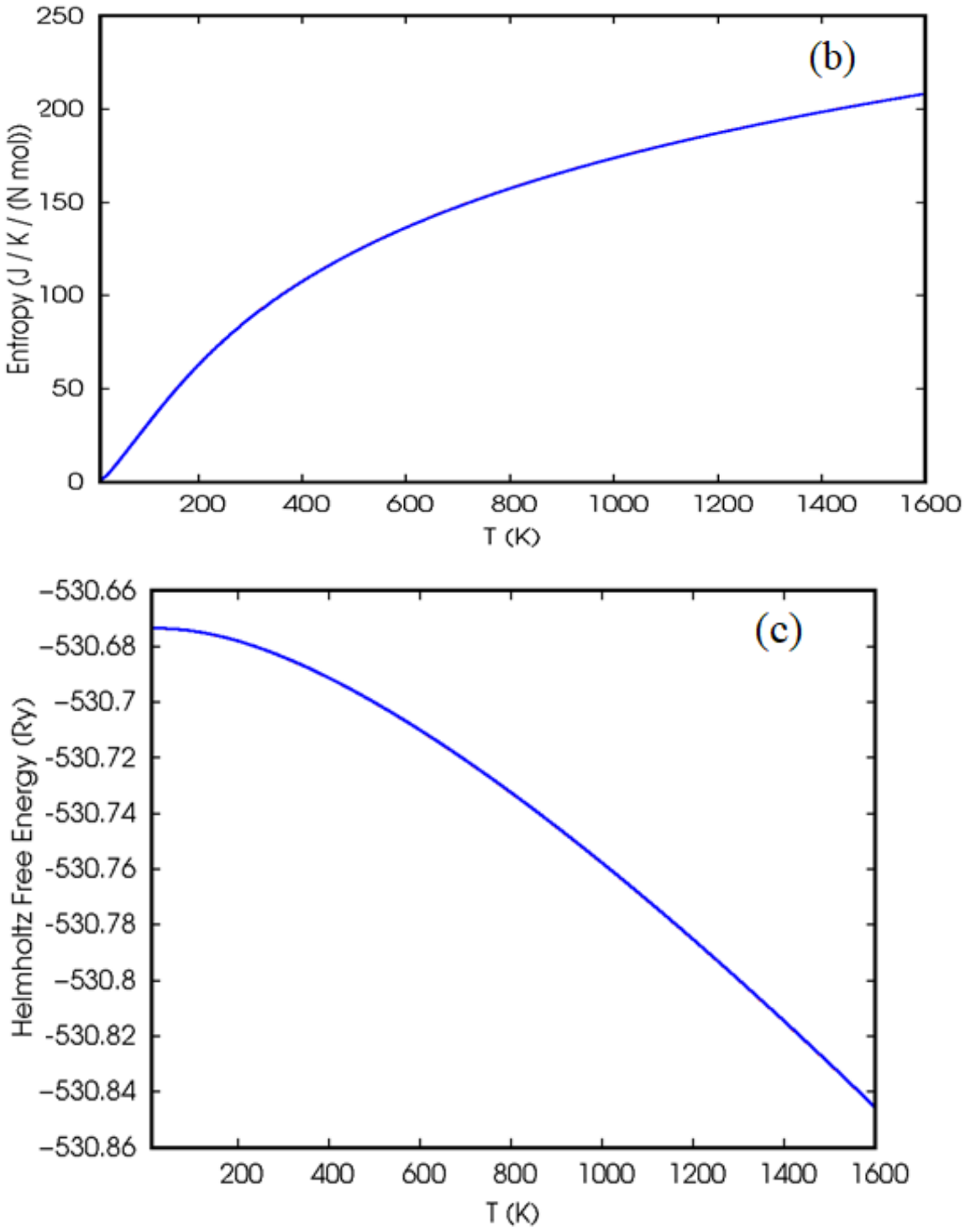

Fig. 11. (a) Dependence of specific heat capacity on the temperature at constant volume, (b) Entropy of the alloy, and (c) Helmholtz free energy

Conclusion

We have explored the structural, electronic, lattice dynamics, optical, thermodynamic, and transport properties of ScAgC half Heusler alloy with and without spin-orbit coupling. We investigated the structural and electronic properties using the generalized gradient approximation based on the density functional theory. The results we obtained for the fundamental lattice parameter for the γ – phase align with results from previous work for

calculations without SOC. Still, the lattice bandgap is wider with SOC calculation. The transport properties calculated using the Bolztrap code suggest that the n-type ScAgC is a better thermoelectric material than the p-type. The n-type semiconductor result is obtained when the spin-orbit coupling is considered in the calculation; otherwise, the p-type semiconductor is promoted. The optical properties show a high absorption coefficient, which increased from 7×10^4 cm^{-1} to 39×10^4 cm^{-1} through the visible light region. The results show that ScAgC absorbs light in the ultraviolet and visible regions. The plasmon frequency for ScAgC alloy is 14.49 eV, positioning it as a promising material for solar cell application. The lattice dynamics and thermodynamic investigation shows that the alloy is stable at low/medium temperatures but unstable at high temperatures. The clear wide phonon band gap between the acoustic and optical branches supports a strong ionic bonding that suggests the material is rigid.

Funding
This work is funded by the National Research Fund (NRF), Tertiary Education Trust Fund, [NRF/SETI/PAE/00068], 2021

Conflict of Interest

The authors declare that they do not have any conflict of interest.

References

[1] Nakamura, J., Asano, N., Hieda, T., Okamoto, C., Katayama, H., & Nakamura, K. (2014). Development of heterojunction back contact Si solar cells. *IEEE Journal of Photovoltaics*, *4*(6), 1491-1495.

[2] Eperon, G. E., Burlakov, V. M., Docampo, P., Goriely, A., & Snaith, H. J. (2014). Morphological control for high performance, solution-processed planar heterojunction perovskite solar cells. *Advanced functional materials*, *24*(1), 151-157.

[3] Wang, H., Liu, H., Dong, Z., Song, T., Li, W., Zhu, L., ... & Chen, H. (2021). Size mismatch induces cation segregation in CsPbI3: Forming energy level gradient and 3D/2D heterojunction promotes the efficiency of carbon-based perovskite solar cells to over 15%. *Nano Energy*, *89*, 106411.

[4] Hasan, A. A., Ahmed Alkahtani, A., Shahahmadi, S. A., Nur E. Alam, M., Islam, M. A., & Amin, N. (2021). Delamination-and electromigration-related failures in solar panels—a review. *Sustainability*, *13*(12), 6882.

[5] Richhariya, G., Meikap, B. C., & Kumar, A. (2022). Review on fabrication methodologies and its impacts on performance of dye-sensitized solar cells. *Environmental Science and Pollution Research*, 1-19.

[6] Heusler, A., & Ranisch, W. (Eds.). (1903). *Eddica minora: Dichtungen eddischer Art aus den Fornaldarsögur und nderen Prosawerken*. W. Ruhfus.

[7] De Groot, R. A., Mueller, F. M., Van Engen, P. G., & Buschow, K. H. J. (1983). New class of materials: half-metallic ferromagnets. *Physical Review Letters*, *50*(25), 2024.

[8] Casper, F., Graf, T., Chadov, S., Balke, B., & Felser, C. (2012). Half-Heusler compounds: novel materials for energy and spintronic applications. *Semiconductor Science and Technology*, *27*(6), 063001.

[9] Anand, S., Xia, K., Hegde, V. I., Aydemir, U., Kocevski, V., Zhu, T., ... & Snyder, G. J. (2018). A valence balanced rule for discovery of 18-electron half-Heuslers with defects. *Energy & Environmental Science*, *11*(6), 1480-1488.

[10] Vikram, Sahni, B., Barman, C. K., & Alam, A. (2019). Accelerated discovery of new 8-electron half-Heusler compounds as promising energy and topological quantum materials. *The Journal of Physical Chemistry C*, *123*(12), 7074-7080.

[11] Mehnane, H., Bekkouche, B., Kacimi, S., Hallouche, A., Djermouni, M., & Zaoui, A. (2012). First-principles study of new half Heusler for optoelectronic applications. *Superlattices and Microstructures*, *51*(6), 772-784.

[12] Kacimi, S.; Mehnane, H.; Zaoui, A. (2014). *I–II–V and I–III–IV half-Heusler compounds for optoelectronic applications: Comparative ab initio study. Journal of Alloys and Compounds, 587(), 451–458.* doi:10.1016/j.jallcom.2013.10.046

[13] Belmiloud, N., Boutaiba, F., Belabbes, A., Ferhat, M., & Bechstedt, F. (2016). Half-Heusler compounds with a 1 eV (1.7 eV) direct band gap, lattice-matched to GaAs (Si), for solar cell application: A first-principles study. *physica status solidi (b)*, *253*(5), 889-894.

[14] Giannozzi, P., Baroni, S., Bonini, N., Calandra, M., Car, R., Cavazzoni, C., ... & Wentzcovitch, R. M. (2009). QUANTUM ESPRESSO: a modular and open-source software project for quantum simulations of materials. *Journal of physics: Condensed matter*, *21*(39), 395502.

[15] Kresse, G., & Joubert, D. (1999). From ultrasoft pseudopotentials to the projector augmented wave method. *Physical review b*, *59*(3), 1758.

[16] Perdew, J. P., Burke, K., & Ernzerhof, M. (1996). Generalized gradient approximation made simple. *Physical review letters*, *77*(18), 3865.

[17] Monkhorst, H. J., & Pack, J. D. (1976). Special points for Brillouin-zone integrations. *Physical review B*, *13*(12), 5188.

[18] Marzari, N., & Vanderbilt, D. (1997). Maximally localized generalized Wannier functions for composite energy bands. *Physical review B*, *56*(20), 12847.

[19] Murnaghan, F. D. (1944). The compressibility of media under extreme pressures. *Proceedings of the National Academy of Sciences*, *30*(9), 244-247.

[20] Birch, F. (1947). Finite elastic strain of cubic crystals. *Physical review*, *71*(11), 809.

[21] Murnaghan, F. D. (1937). Finite deformations of an elastic solid. *American Journal of Mathematics*, *59*(2), 235-260.

[22] Kokalj, A. (1999). XCrySDen—a new program for displaying crystalline structures and electron densities. *Journal of Molecular Graphics and Modelling*, *17*(3-4), 176-179.

[23] Togo, A., & Tanaka, I. (2015). First-principles phonon calculations in materials science. *Scripta Materialia*, *108*, 1-5.

[24] Methfessel, M. P. A. T., & Paxton, A. T. (1989). High-precision sampling for Brillouin-zone integration in metals. *Physical Review B*, *40*(6), 3616.

[50] Öğüt, S., & Rabe, K. M. (1995). Band gap and stability in the ternary intermetallic compounds NiSnM (M= Ti, Zr, Hf): A first-principles study. *Physical Review B*, *51*(16), 10443.

[51] Khein, A., Singh, D. J., & Umrigar, C. J. (1995). All-electron study of gradient corrections to the local-density functional in metallic systems. *Physical Review B*, *51*(7), 4105.

[52] Aliev, F. G., Brandt, N. B., Moshchalkov, V. V., Kozyrkov, V. V., Skolozdra, R. V., & Belogorokhov, A. I. (1989). Gap at the Fermi level in the intermetallic vacancy system RBiSn (R= Ti, Zr, Hf). *Zeitschrift für Physik B Condensed Matter*, *75*(2), 167-171.

[53] Ozisik, H. B., Ateser, E., Ozisik, H., Colakoglu, K., & Deligoz, E. (2017). Ab-initio calculations on half-Heusler NiXSn (X= Zr, Hf) compounds: electronic and optical properties under pressure. *Indian Journal of Physics*, *91*(7), 773-778.

[54] Zou, D. F., Xie, S. H., Liu, Y. Y., Lin, J. G., & Li, J. Y. (2013). Electronic structure and thermoelectric properties of half-Heusler $Zr_{0.5}Hf_{0.5}NiSn$ by first-principles calculations. *Journal of Applied Physics*, *113*(19), 193705.

[55] M Ahmad, N Ullah, G Murtaza, R Khenata, S Bin Omran and A Bouhemadou J. Magn. Magn. Mater. 377 204–210 (2015)

[56] Denault, K. A., Brgoch, J., Kloß, S. D., Gaultois, M. W., Siewenie, J., Page, K., & Seshadri, R. (2015). Average and local structure, Debye temperature, and structural rigidity in some oxide compounds related to phosphor hosts. *ACS applied materials & interfaces*, *7*(13), 7264-7272.

[57] Zhuo, Y., Mansouri Tehrani, A., Oliynyk, A. O., Duke, A. C., & Brgoch, J. (2018). Identifying an efficient, thermally robust inorganic phosphor host via machine learning. *Nature communications*, *9*(1), 1-10.

[58] Cai, X., Zhang, Y., Shi, Z., Chen, Y., Xia, Y., Yu, A., ... & Zhang, H. (2022). Discovery of Lead-Free Perovskites for High-Performance Solar Cells via Machine Learning: Ultrabroadband Absorption, Low Radiative Combination, and Enhanced Thermal Conductivities. *Advanced Science*, *9*(4), 2103648.

[59] Toher, C., Plata, J. J., Levy, O., De Jong, M., Asta, M., Nardelli, M. B., & Curtarolo, S. (2014). High-throughput computational screening of thermal conductivity, Debye temperature, and Grüneisen parameter using a quasiharmonic Debye model. *Physical Review B*, *90*(17), 174107.

[60] Osafile, O. E., & Nenuwe, O. N. (2021). Lattice Dynamics and thermodynamic Responses of XNbSn Half-Heusler Semiconductors: A First-Principles Approach. *Journal of the Nigerian Society of Physical Sciences*, 121-130.